




Article

Multiresolution Topology Optimization of Large-Deformation Path-Generation Compliant Mechanisms with Stress Constraints

Joseph Reinisch ^{1,2} , Erich Wehrle ^{1,*}  and Johannes Achleitner ^{1,2} 

¹ Free University of Bozen-Bolzano, Universitätsplatz 5, 39100 Bozen, Italy; Joseph.Reinisch@tum.de (J.R.); Johannes.Achleitner@tum.de (J.A.)

² Institute of Aircraft Design, Technical University of Munich, 15 85748 Garching bei München, Germany

* Correspondence: Erich.Wehrle@unibz.it

Abstract: Topology optimization is a powerful numerical tool in the synthesis of lightweight structures and compliant mechanisms. Compliant mechanisms present challenges for topology optimization, as they typically exhibit large displacements and rotations. Path-generation mechanisms are a class of mechanisms that are designed to follow an exact path. The characteristics of compliant mechanisms therefore exclude the validity of linear finite-element analysis to ensure the proper modeling of deformation and stresses. As stresses can exceed the limit when neglected, stress constraints are needed in the synthesis of compliant mechanisms. Both nonlinear finite-element analysis as well as the consideration of stress constraints significantly increase computational cost of topology optimization. Multiresolution topology optimization, which employs different levels of discretization for the finite-element analysis and the representation of the material distribution, allows an important reduction of computational effort. A multiresolution topology optimization methodology is proposed integrating stress constraints based on nonlinear finite-element analysis for path-generation mechanisms. Two objective formulations are used to motivate and validate this methodology: maximum-displacement mechanisms and path-generation mechanisms. The formulation of the stress constraints and their sensitivities within nonlinear finite-element analysis and multiresolution topology optimization are explained. We introduce two academic benchmark examples to demonstrate the results for each of the objective formulations. To show the practical, large-scale application of this method, results for the compliant mechanism structure of a droop-nose morphing wing concept are shown.



Citation: Reinisch, J.; Wehrle, E.; Achleitner, J. Multiresolution Topology Optimization of Large-Deformation Path-Generation Compliant Mechanisms with Stress Constraints. *Appl. Sci.* **2021**, *11*, 2479. <https://doi.org/10.3390/app11062479>

Academic Editor: Yuzo Nakamura

Received: 10 December 2020

Accepted: 28 February 2021

Published: 10 March 2021

Publisher's Note: MDPI stays neutral with regard to jurisdictional claims in published maps and institutional affiliations.



Copyright: © 2021 by the authors. Licensee MDPI, Basel, Switzerland. This article is an open access article distributed under the terms and conditions of the Creative Commons Attribution (CC BY) license (<https://creativecommons.org/licenses/by/4.0/>).

Keywords: topology optimization; compliant mechanisms; nonlinear finite-element analysis; path generation; stress constraints; multiresolution; sensitivity analysis

1. Introduction

Engineers are constantly pursuing the design of lighter, faster and more efficient structures and mechanisms. Here, we use structural design optimization—and more specifically topology optimization—to design optimal lightweight compliant mechanisms. These flexible structures have the same design goals as more traditional mechanisms, though without joints. Instead, the motion of the mechanism is achieved by elastic deformation. This characteristic presents a number of advantages including no frictional loss, scalability and precision due to lack of backlash [1]. Further, the energy required for movement can be saved as elastic energy, which can be used to move the mechanism back to its original position or to be harvested in the form of electricity, e.g., Rojas et al. [2]. The optimal designs achieved via topology optimization have traditionally undergone toilsome derivation of geometries to ensure manufacturability. This can be now (partially) avoided with additive manufacturing techniques in which the optimal results are directly fabricated.

As compliant mechanisms are then of one material without joints, it can be seen as being a monolithic design, which reduces manufacturing expense as no assembly is necessary.

As compliant mechanisms typically exhibit large displacements and rotations, the standard method of topology optimization with linear elastostatic finite-element analysis (FEA) is deemed to be inadequate in such cases. Further, trajectories of path-generation mechanisms typically do not correlate to linear deformation, which also necessitates nonlinear FEA. Stress must be included as a constraint in the design optimization problem as its values can exceed physical limits, if neglected. In the following, we propose a method for the synthesis of both maximum-displacement and path-generating compliant mechanisms with multilevel stress-constrained topology optimization based on geometrically nonlinear finite-element analysis.

Topology optimization is the optimal placement of material, which can trace its origins to the analytical work of [3]. As the design problem is inherently discrete, i.e., material is present or not, the algorithmic handling of this problem is a challenge. Topology optimization in its modern form stems from the homogenization method of Bendsoe and Kikuchi [4] and the Solid Isotropic Material with Penalization (SIMP) by Bendsoe [5]. SIMP “continualizes” the design space by allowing for intermediate states of material between full and void, typically controlled via density. Although the continualization of the design space is an efficient solution for the discrete problem, it comes with a number of further problems, including checkerboarding, possible local minima and mesh-dependent results [6].

Further methods have been devised to handle the topology optimization problems, outlined by Sigmund [7]. Non-gradient-based methods include the Soft Kill Option (SKO) by Baumgartner et al. [8] and the use of hybrid cellular automata (HCA) by Tovar [9]. Due to the large number of design variables in topology optimization, first-order algorithms have proven their efficiency, especially in terms of avoiding the forming of the Hessian, as is the case with second-order algorithms. Therefore, the concentration here is on the use of first-order optimization algorithms to ensure efficiency. The first-order optimization algorithm, method of moving asymptotes (MMA), first introduced by Svanberg [10], is the specific algorithm used here.

In contrast to the “standard” topology optimization objective of minimum compliance (i.e., minimum strain energy and therefore maximum stiffness), compliant structures are designed for flexibility of one or more degrees of freedom. The first topology optimization approach for the synthesis of compliant mechanisms was introduced by Ananthasuresh et al. [11], which was followed by Sigmund [12]. The topology optimization approach for such compliant structures is reviewed by Zhu et al. [13]. This review highlights the lack of literature in the field of topology optimization for compliant mechanisms with large deformation and stress constraints, which we address here.

In the present work, two types of this design problem are considered, both introduced by Pedersen et al. [14]:

Problem type I: The design of maximum-displacement mechanisms finds the topology for the largest displacement of predefined degrees of freedoms for a given load.

Problem type II: The design of path-generation mechanisms finds the topology in which certain degrees of freedom are designed to go through predefined points (also known as way points or precision points), which describe a trajectory or path.

As large deformations—and therefore nonlinear strains—are desired in compliant mechanisms, nonlinear finite-element analysis is required for their design [14]. The nonlinear structural–mechanical analysis, which serves as the basis of the topology optimization, can be split into two general categories: static (including quasi-static) and transient analysis. A proposal for the categorization of the methods of topology optimization was introduced by Wehrle et al. [15]. This categorization includes the replacement of the nonlinear behavior with a series of linear calculations via the update method from Park [16] or a single replacement load introduced by Volz [17], Duddeck and Volz [18]. Other methods utilize efficient

gradient-free rule-based methods, e.g., hybrid cellular automata by Duddeck et al. [19], avoiding the challenge of deriving and implementing sensitivity analysis for nonlinear finite-element analysis. The behavior of compliant mechanisms in this work is considered quasi-static. Studies on path-generation compliant mechanisms by Dirksen et al. [20] and Chen et al. [21] include large deformations, yet neglect stress constraints. As compliant mechanisms are designed to avoid plastic behavior, the authors find the application of stress constraints necessary and therefore extend this study to include them in this work. The material may also exhibit nonlinear elasticity, though this will not be considered. Therefore, we will restrict our examples to topology optimization for stress-constrained compliant mechanisms using nonlinear quasi-static analysis considering linear-elastic material models and its sensitivity analysis.

In order to obtain high-resolution topologies with the classical topology optimization approach, a high number of finite elements is required and with it a high computational cost. Nonlinear finite-element analysis exacerbates the high computational effort, as the case in this work. Standard topology optimization assigns a material density to each finite element and hence the element size defines the minimum length scale for the topology to be found. Multiple approaches were proposed to reduce computational effort in topology optimization e.g., adaptive mesh refinement [22,23] or domain decomposition [24]. Nguyen et al. [25,26] introduced a multiresolution topology optimization (MTO) scheme, which decouples the degree of detail of the topology from the finite-element size. Therefore, different discretizations for displacements, densities and design variables are used. By this means, it is possible to obtain detailed designs on a relatively coarse FE mesh. In this work, multiresolution topology optimization is extended with stress constraints and used for the synthesis of large-deformation path-generating compliant mechanisms.

There are several challenges when considering stress constraints in topology optimization. Low density elements can show singular behavior resulting in exaggerated stresses, which then dominate the progression of the topology optimization. Duysinx and Sigmund [27] introduced a relaxed stress scheme to avoid this problem. De Leon et al. [28] as well as Conlan-Smith [29] implemented stress constraints in the synthesis of compliant mechanisms with topology optimization, albeit only for linear finite-element analysis. This was then expanded in the work by De Leon et al. [30] for nonlinear finite-element analysis and was applied to the maximum displacement objective. A further problem is that stress is a field variable varying for each element and hence necessitating for a large number of constraints. A common approach avoids a large number of constraint functions by use of function aggregation methods. Global stress measures approximating the maximum stress include the Kreisselmeier–Steinhauser function and the p-norm (cf. Duysinx and Sigmund [27], Kreisselmeier and Steinhauser [31], Yang and Chen [32], Martins and Poon [33], Le et al. [34], Verbart et al. [35]). The present work will utilize the latter, which will include the elements stress fields. These are approximated by the stress value averaged at the element centroids.

Building upon the works described above, the present work extends topology optimization to achieve the design of path-generation mechanisms while constraining the maximum stress. The methodology will be described with the synthesis of maximum-displacement and path-generation compliant mechanisms. Further novelty of this work includes the multiresolution topology optimization under stress constraints with geometrically nonlinear finite-element analysis. Benchmark examples are followed by an engineering example, which shows the design of the mechanism driving a morphing wing. This engineering example demonstrates the large-scale practicality of the method developed. Finally, we conclude with a summary and outlook.

2. Topology Optimization for the Synthesis of Compliant Mechanisms

In the following, the proposed stress-constrained multiresolution topology optimization methodology for the synthesis of compliant mechanisms (Problem types I and II) will be introduced.

2.1. Nonlinear Finite-Element Analysis

The central part of topology optimization is structural–mechanical analysis, which is the basis of the values for the optimization functions (objective and constraints) of each optimization iteration. This analysis is carried out discretizing the solution space of the governing equations. The equations describing the nonlinear structural analysis are briefly introduced here. A geometrically nonlinear finite-element method using plane stress and a total Lagrangian formulation [36,37] is utilized, which was implemented by Reinisch [38,39] and further developed by Grosse [40].

Equilibrium is defined as

$$\underline{R} = \underline{P}_{\text{int}} - \underline{P}_{\text{ext}} = \underline{0}, \tag{1}$$

where \underline{R} is the vector of residuals, $\underline{P}_{\text{ext}}$ is the external force vector and $\underline{P}_{\text{int}}$ is the internal force vector. The internal force vector is defined element-wise, given here for the i th element by

$$\underline{P}_{\text{int},i} = \int_{\Omega_i} \underline{B}_{L,i}^T \underline{\bar{F}}_i \underline{\sigma}_{2PK,i} dV. \tag{2}$$

The notation here denotes vectors as underlined symbols, matrices as double underlined symbols and scalars as symbols without an underline. It should be noted that we will use Voigt notation unless otherwise denoted.

For the deformation gradient tensor, we will use both tensor and Voigt notations, the matrix $\underline{\bar{F}}$ and the vector $\underline{\tilde{F}}$,

$$\underline{\bar{F}} = \begin{bmatrix} F_{11} & 0 & F_{12} \\ 0 & F_{22} & F_{21} \\ 0 & F_{12} & F_{11} \\ F_{21} & 0 & F_{22} \end{bmatrix}, \quad \underline{\tilde{F}} = \begin{bmatrix} F_{11} \\ F_{22} \\ F_{12} \\ F_{21} \end{bmatrix}. \tag{3}$$

The operator matrix $\underline{B}_{L,i}$ in Equation (2) corresponds to the derivative of $\underline{\tilde{F}}_i$ with respect to the element nodal displacement vector \underline{u}_i . The second Piola–Kirchhoff stress vector $\underline{\sigma}_{2PK,i}$ is defined in Equation (5). As geometric nonlinearity is considered, nonlinear Green–Lagrange strains are calculated for the i th element,

$$\underline{\varepsilon}_{GL,i} = \frac{1}{2} \left(\underline{\bar{F}}_i^T \underline{\tilde{F}}_i - \begin{bmatrix} 1 \\ 1 \\ 0 \end{bmatrix} \right), \tag{4}$$

and the second Piola–Kirchhoff stresses, which are conjugate to Green–Lagrange strains, are

$$\underline{\sigma}_{2PK,i} = \underline{C}_{VK} \underline{\varepsilon}_{GL,i}, \tag{5}$$

where \underline{C}_{VK} is the linear-elastic Saint Venant–Kirchhoff constitutive matrix for plane stress.

The nonlinear equilibrium Equation (1) is solved using the iterative Newton–Raphson approach by sequential linearization. Therefore, in each iteration j , we solve the linear system

$$\underbrace{\frac{\partial \underline{R}}{\partial \underline{u}}}_{\underline{K}_T} \Delta \underline{u}^{(j+1)} = -\underline{R}(\underline{u}^{(j)}), \tag{6}$$

where \underline{K}_T is the tangent stiffness matrix equal to $\frac{\partial \underline{R}}{\partial \underline{u}}$. We then update the displacement vector of the j th iteration $\underline{u}^{(j)}$ by the resulting displacement increment $\Delta \underline{u}^{(j+1)}$. This process is continued until reaching convergence at the equilibrium state $\underline{R} \approx \underline{0}$ within a set tolerance.

As the second Piola–Kirchhoff stress lacks physical meaning, it is transformed into Cauchy stress σ_C after obtaining the equilibrium deformation state. This transformation is shown for simplicity purposes with the use of matrix notation to describe the stress tensors,

$$\underline{\sigma}_{C,i} = \frac{1}{J_i} \underline{F}_i \underline{\sigma}_{2PK,i} \underline{F}_i^T, \tag{7}$$

where J is the determinant of the deformation gradient \underline{F} and is a measure for the volumetric change. It should be noted that due to plane stress, the component F_{33} governed by the Poisson effect must also be considered for the derivation of the determinant of the deformation gradient. If it is not considered, the plain strain assumption would be applied.

In this study, bilinear quadrilateral finite elements are used and the integrals are approximated by four Gauss integration points. The stress fields of interest are obtained by evaluation of the element Cauchy stresses $\underline{\sigma}_{C,i}$ at the element centroid.

2.2. Formulation of Topology Optimization

In the formulation of numerical optimization, the objective function f is minimized, while maintaining that the constraint functions g_i are not violated. The optimization is carried out here with the first-order algorithm *method of moving asymptotes* (MMA) Svanberg [10].

2.2.1. Design Variables and Their Stabilization

In density-based topology optimization, as is the case in this work, the design variables x_i represent the element densities, which are scaled between zero for a void and unity for full material,

$$x_i \in [0, 1]. \tag{8}$$

The design variables are mapped to the Young’s modulus of each element using the value for the base material E_0 via the modified SIMP formulation [41],

$$E_i = E_{\min} + (E_0 - E_{\min})x_i^\theta. \tag{9}$$

The inclusion of a minimum value for the Young’s modulus E_{\min} avoids numerical singularities in the finite-element analysis that occur when elements have numerically zero stiffness. The value θ penalizes the design space of intermediate densities between solid and void is $\theta = 3$ as commonly used in the literature (cf. Sigmund [12], Pedersen et al. [14], De Leon et al. [28]).

To avoid mesh-dependent results and checkerboarding, the design variables are further filtered using the density filtering method introduced by Bruns and Tortorelli [42]. This filtering approach is defined according to Sigmund [41] by

$$\tilde{x}_i = \frac{\sum_{j \in \mathbb{N}_i} H_{ij} V_j x_j}{\sum_{j \in \mathbb{N}_i} H_{ij} V_j}, \tag{10}$$

where V_j is the volume of the j th element and H_{ij} is a cone-shaped weighting function of the form

$$H_{ij} = \max\{0, r_{\min} - \Delta(i, j)\}. \tag{11}$$

The filter radius is denoted by r_{\min} and $\Delta(i, j)$ represents the distance between the centroids of the i th and the j th element. In addition to the filter, we apply a Heaviside projection scheme according to Guest et al. [43], using the following step approximation:

$$\bar{x}_i = \frac{\tanh(\beta\eta) + \tanh(\beta(\tilde{x}_i - \eta))}{\tanh(\beta\eta) + \tanh(\beta(1 - \eta))}. \tag{12}$$

This is applied in order to avoid so-called intermediate “gray solutions”, i.e., intermediate density elements in-between solid and void regions. The projection parameters β and

η define the degree of discreteness of the step between solid, void and its threshold value. For the results presented below, $\eta = 0.2$ is chosen and the parameter β is sequentially increased over the number of optimization iterations j from an initial value of $\beta_0 = 1$ to the final value of $\beta_{\max} = 150$,

$$\beta_j = \beta_0 2^{\frac{j-1}{30}}. \quad (13)$$

The resulting modified design variables \bar{x}_i of Equation (12) replace the original design variables x_i in Equation (9) and, hence, determine the finite-elements stiffness properties.

Another difficulty regarding topology optimization using nonlinear finite-element analysis is the numerical instability of low-density elements. With linear FEA, singularity of the stiffness matrix is avoided by introducing E_{\min} in to the SIMP approach. In nonlinear analysis, this approach only stabilizes the first equilibrium iterations. For the following load steps, large deformations of the low stiffness elements cause negative element volumes and the singularity problems still occur. As a consequence, convergence is heavily disturbed.

Several approaches to resolve this issue are reported in literature. Bruns and Tortorelli [42] and De Leon et al. [30] suggested to use hyperelastic material laws with increased stiffness at high deformations instead of the Saint Venant–Kirchhoff law. Pedersen et al. [14] reported, that the approach of Bruns and Tortorelli was unsuccessful resolving the issues for their numerical examples. They instead excluded low density elements from the convergence checks of the Newton–Raphson iteration. Bruns and Tortorelli [44] introduced an element deletion and reintroduction scheme for low density elements. Yoon and Kim [45] approached the issues by introducing linear springs, which provide an interconnection between the elements. The spring stiffnesses are used as design variables and the elements kept solid and can be thus either nonlinear or linear element formulation.

Wang et al. [46] proposed to exclude the nonlinear strain energy terms in low density regions and further developed this approach in Wang et al. [47]. A modified version of the method introduced by Wang et al. [47] is used in this study originating from Reinisch [38]. For low density elements, linear strain energy terms W_L are used. These are then interpolated towards a full nonlinear strain energy term W_{NL} in the solid regions,

$$W_i = W_{NL}(\gamma_i \underline{u}_i) - W_L(\gamma_i \underline{u}_i) + W_L(\underline{u}_i). \quad (14)$$

The interpolation term $\gamma_i \in [0, 1]$ is defined similarly to the projection method in Equation (12) as a Heaviside function approximation,

$$\gamma_i = \frac{\tanh(\beta_1 \eta_1) + \tanh(\beta_1 ((\bar{x}_i - x_{\text{off}})^\theta - \eta_1))}{\tanh(\beta_1 \eta_1) + \tanh(\beta_1 (1 - \eta_1))}, \quad (15)$$

where β_1 and η_1 are step parameters, x_{off} is an additional offset parameter introduced and θ is the penalization exponent term. The term x_{off} shifts the cutoff further toward $\bar{x} = 0$ in order to limit the number of elements in which linear strain energy is used. The results presented in this work are obtained using the parameters $\beta_1 = 500$, $\eta_1 = 0.01$ and $x_{\text{off}} = 0.2$.

2.2.2. Maximum Displacement Objective Function

The first objective under consideration is the maximum displacement objective f_u in which the displacement of one or more degrees of freedom is maximized (problem type I). This is defined as Pedersen et al. [14]

$$f_u = -u_{\text{out}} = -\underline{L}^T \underline{u} \quad (16)$$

where \underline{u} is the column vector of the global displacements and \underline{L} is a column vector with the entry equal to unity at the degree of freedom of interest and elsewhere zero. This results in the scalar value f_u , which equals to the negative of the displacement of interest u_{out} .

2.2.3. Path Generation Objective Function

The second objective formulation presented is the path-generation objective f_{path} (problem type II) introduced by Pedersen et al. [14]. Here, m precision points \underline{u}^* are chosen, through which a predefined output node shall pass for given input displacement values $\underline{u}_{\text{in},j}$ at input node j . Therefore, the objective function f_{path} is defined by

$$f_{\text{path}} = \sum_{i=0}^n \alpha_i \sum_{j=1}^m \sum_{k=1}^l (\underline{L}_k^T \underline{u}_{i,j} - u_{k,j}^*)^2. \quad (17)$$

As with the maximum displacement objective function, \underline{L} also has all zero entries except for a single entry that is equal to unity. By this means, the output displacement of interest is obtained from the global displacement vector by $u_{\text{out}} = \underline{L}^T \underline{u}$. As described by Pedersen et al. [14], in order to achieve load-carrying black-and-white solutions, n additional load cases with counter loads acting at the output node are applied. These load cases are considered by the first summation term i in Equation (17), with α being a weighting factor. For $i = 0$, the original load case with no counter loads is considered. The innermost sum over k takes into account that at the output node the output displacements $u_{k,j}^*$ are prescribed for l different degrees of freedom and for each precision point (the sum over j). Hence, the objective function represents the weighted sum of squared errors of position of the control points under all specified load cases. A topology is therefore sought in which the output node displacement most closely approximates the prescribed path for the given input displacement sequence.

2.2.4. Volume Constraint

The maximum amount of material to be used is given via volume fraction φ with respect to the volume of full material of the design domain V_{tot} ,

$$\varphi = \frac{\bar{\mathbf{x}}^T \underline{V}}{V_{\text{tot}}} = \frac{V_{\text{util}}}{V_{\text{tot}}}, \quad (18)$$

where \underline{V} is the vector of element volumes. The volume constraint function is normalized and takes the form

$$g_V = \frac{\varphi}{\varphi_{\text{allow}}} - 1, \quad (19)$$

where φ_{allow} is the allowable volume fraction.

2.2.5. Stress Constraint

Although large displacements, deformations and rotations are present and even desired, permanent, i.e., plastic deformation is to be avoided. Compliant mechanisms are often designed for cases that induce cyclic loading that may require consideration of the fatigue strength (though outside the scope of the present work). Therefore, stress constraints must be considered in topology optimization to guarantee the integrity of a compliant device.

As shown by De Leon et al. [28], stress constraints also prevent—in part—so-called one-node joints (or hinges). This is a common problem in topology optimization for compliant structures as one-node joints allow for large displacements in the simulation, but are not feasible in real world continuous (hingeless) structures. One can say that one-node joints are analogous to checkerboarding in more traditional topology optimization for minimum compliance. Stress constraints hinder the topology optimization from moving in this direction. They can prevent the appearance of one-node hinges by limiting the stresses in two neighboring low-density elements evolving next to the center node. A complete elimination of one-node hinges solely by the use of the stress constraint formulation introduced below is, though, not possible as these elements can show deformation without notable resulting stress (cf. Equation (20)).

If stress constraints are applied, the design problem limits the stress in the entire design domain, including those of voids. To avoid having exaggerated and nonphysical high stresses in elements of low element density, which then dominate the optimization problem, we define the relaxed stress of the von Mises equivalent stress σ_M for each element i as introduced by Duysinx and Sigmund [27], Le et al. [34],

$$\tilde{\sigma}_i = \bar{x}_i^q \sigma_{M,i}, \tag{20}$$

which uses a relaxation constant q . In contrast to De Leon et al. [28], in which best convergence is achieved using a constant parameter of $q = 0.5$, the most stable convergence behavior for the examples presented here was obtained starting with $q = 1$ and reducing this parameter gradually to its final value of $q = 0.5$ early in the optimization. This is done starting from the 20th iteration from which q is reduced by 0.05 at every 10th iteration. The von Mises stresses σ_M are obtained from the elemental Cauchy stress vectors $\underline{\sigma}_C$ (evaluated at the element centroids) by

$$\sigma_{M,i} = \sqrt{\underline{\sigma}_{C,i}^T \underline{A} \underline{\sigma}_{C,i}}, \tag{21}$$

where the expression \underline{A} is the auxiliary matrix of the form

$$\underline{A} = \begin{bmatrix} 1 & -0.5 & 0 \\ -0.5 & 1 & 0 \\ 0 & 0 & 3 \end{bmatrix}. \tag{22}$$

As a low number of stress constraints is needed for algorithm efficiency, the maximum stress is constrained globally in a single aggregated constraint function. The aggregation is carried out via a continuous approximation of the maximum operator, the so-called p-norm Yang and Chen [32], Le et al. [34], defined by

$$\sigma_{\max} \approx \sigma_p = \left(\sum_i V_i \tilde{\sigma}_i^p \right)^{\frac{1}{p}}, \tag{23}$$

where σ_p is the p-norm of the stress, V_i is the volume of each element and p is the constant p-norm parameter. For $p = \infty$, the function takes the maximum, and here it is chosen as $p = 12$. We further use a normalization scheme proposed by Le et al. [34], allowing a correction of the global stress measure in accordance to the quality of its estimate in the prior iteration.

$$\hat{\sigma}_p = c_k \sigma_p. \tag{24}$$

We obtain the normalization parameter c in the k th iteration by solving

$$c_k = \frac{1}{2} \left(\frac{\sigma_{\max,(k-1)}}{\sigma_{p,(k-1)}} + c_{k-1} \right), \tag{25}$$

where $\sigma_{\max,(k-1)}$ is the maximum von Mises equivalent stress in the previous iteration and $c_0 = 1$ is the starting value. The complete equation for the normalized p-norm of the relaxed equivalent stress in the k th iteration is

$$\hat{\sigma}_{p,k} = c_k \left(\sum_i V_i \left(\bar{x}_i^q \sigma_{M,i} \right)^p \right)^{\frac{1}{p}}, \tag{26}$$

from which we formulate the stress constraint used in the topology optimization,

$$g_\sigma(\underline{x}) = \frac{\hat{\sigma}_{p,k}}{\sigma_{\text{allow}}} - 1. \tag{27}$$

2.2.6. Multiresolution Topology Optimization

The multiresolution topology optimization (MTOP) formulation was introduced by Nguyen et al. [25] and reduces the computational cost necessary for the calculation of high resolution topologies. Since the most significant part of the computational cost of topology optimization is finite-element analysis, [25] applies different discretization levels for the displacements (FE analysis), the densities (material representation) and the design variables (optimization). In general, the FE analysis is performed on a coarser mesh, whereas the densities and the design variables are mapped on to finer meshes. By means of this uncoupling of FE displacement elements, densities and design variables, higher resolution results can be obtained with a computational effort comparable to the original solution.

Based on the work of Nguyen et al. [25,26], a new multiresolution topology optimization scheme is proposed, extending to the consideration of stress constraints. In this work the design variable mesh is chosen to be coincident to the density mesh. The key to multiresolution topology optimization is to find a functional relationship between the displacement element's internal force vector and stiffness matrix for structural analysis and the single densities of the density elements. This relationship can be found in the summation terms of the Gauss integration approximation by assigning a density element to each Gauss integration point. By this means, e.g., the internal force vector is approximated as

$$\underline{P}_{\text{int},i} = \int_{\Omega_i} \underline{B}_{L,i}^T \underline{F}_i \underline{C}_{\text{VK},i} \underline{\varepsilon}_{\text{GL},i} dV \approx \sum_{j=1}^{n_{gp}} \underline{P}_{\text{int},i,j} \quad (28)$$

where $\underline{P}_{\text{int},i,j}$ is the integrand for the internal force vector (see Equation (2)) of the displacement element i at the Gauss point j assigned to the corresponding density element. For the derivation of $\underline{P}_{\text{int},i,j}$, the constitutive matrix $\underline{C}_{\text{VK},j}$ of each summation term uses the specific Young's modulus E for the corresponding density element, obtained by the SIMP approach. In Figure 1, an exemplary subdivision of a displacement element (a) in four density elements and its corresponding Gauss integration points (b) are given. The isoparametric element is divided in four equally sized density subelements, each of which influences the summation term of the internal force vector and the tangent stiffness matrix corresponding to the Gauss point within the density elements domain. The number of subelements must be equal to the number of integration points used. For material representation, all the density elements with density values $\bar{x}_{i,j}$ are assembled to a global density mesh. The global density vector $\bar{\underline{x}}$ and hence the design variable vector \underline{x} in this approach are of the size $n_{el} \times n_{gp}$.

The definition of the displacement elements and the global displacement vector \underline{u} for multiresolution topology optimization does not change compared to standard topology optimization. Therefore, the objective function definitions in Equations (16) and (17) remain unchanged also for the multiresolution topology optimization approach.

The utilized volume V_{util} for the calculation of the volume fraction φ defining the volume constraint in Equation (19) is changed for multiresolution topology optimization. It can be expressed by the following summation term:

$$V_{\text{util}} = \sum_{i=1} \sum_{j=1} \bar{x}_{i,j} V_{i,j}, \quad (29)$$

where $\bar{x}_{i,j}$ and $V_{i,j}$ respectively are the density and the volume of the subelement j of the displacement element i .

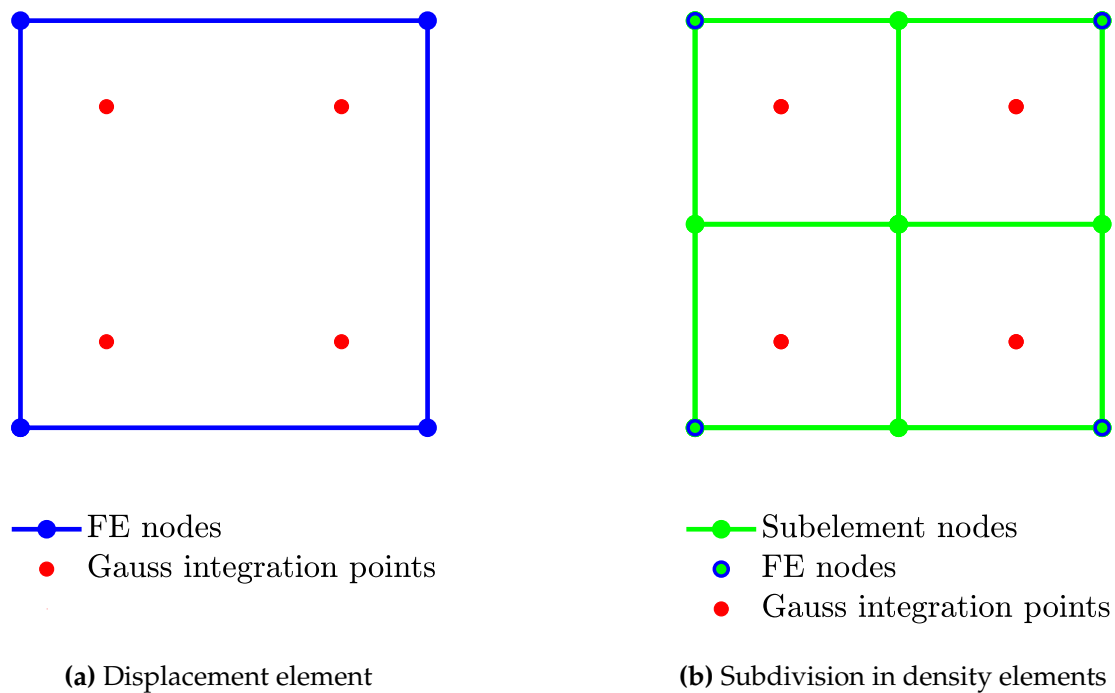


Figure 1. Example of displacement element and density elements for multiresolution topology optimization with four Gauss integration points.

The stress values $\underline{\sigma}_{C,i}$ for the stress constraint formulation of the multiresolution topology optimization are evaluated at the Gauss integration points. The resulting stress values $\underline{\sigma}_{C,i,j}$ at the integration points j are then assigned to the corresponding density element with density $\tilde{x}_{i,j}$. By this means, looking at the example shown in Figure 1 to each density subelement j of the displacement element i , its specific stress value $\underline{\sigma}_{C,i,j}$ is assigned and the aggregated stress measure in Equation (23) is calculated as sum over all the density elements defining the design space.

$$\sigma_{\max} \approx \sigma_p = \left(\sum_i \sum_j V_{i,j} \tilde{\sigma}_{i,j}^p \right)^{\frac{1}{p}}, \tag{30}$$

2.3. Design Sensitivity Analysis via Adjoint Methodology

In topology optimization, the problem is typically formulated with constraint aggregation so that the number of design variables is magnitudes greater than the sum of the number of objectives and constraints. Therefore, an adjoint sensitivity methodology has higher efficiency than direct sensitivity analysis. A thorough reference to sensitivity analysis within the framework of structural design optimization was put forth by Martins and Hwang [48].

The adjoint equations, based on early works by Bliss [49], Goodman and Lance [50], Kelley [51] and further elaborated upon by Michaleris et al. [52], Tortorelli and Michaleris [53], can be derived via Lagrangian multipliers. The Lagrangian multipliers are solved for by taking advantage of the derivatives of the function of interest with respect to the state variable. Below, we show the adjoint sensitivity analysis for an arbitrary functional f used in topology optimization with nonlinear finite-element analysis, which is needed for the specific functionals in the following sections. We define the general functional as

$$f(\underline{u}(x), x) \tag{31}$$

and its total sensitivity as

$$\frac{df}{d\underline{x}} = \frac{\partial f}{\partial \underline{x}} + \frac{\partial f}{\partial \underline{u}} \frac{d\underline{u}}{d\underline{x}}. \tag{32}$$

The adjoint sensitivity analysis based on the Lagrangian equation for a calculation at the k th iteration,

$$\mathcal{L}(\underline{x}, \underline{u}_k, \lambda_k) = f(\underline{x}, \underline{u}_k(\underline{x})) + \lambda_k^T \underline{R}_k(\underline{u}_k(\underline{x}), \underline{x}), \tag{33}$$

to which the functional is added to the vector of Lagrangian multipliers λ multiplied by the vector of residuals \underline{R}_k , which is equal to zero when perfectly converged. The total derivative is

$$\frac{df}{d\underline{x}} \equiv \frac{d\mathcal{L}}{d\underline{x}} = \frac{\partial f}{\partial \underline{x}} + \frac{\partial f}{\partial \underline{u}_k} \frac{d\underline{u}_k}{d\underline{x}} + \lambda_k^T \left(\frac{\partial \underline{R}_k}{\partial \underline{x}} + \frac{\partial \underline{R}_k}{\partial \underline{u}_k} \frac{d\underline{u}_k}{d\underline{x}} \right). \tag{34}$$

After substituting $\frac{\partial \underline{R}_k}{\partial \underline{u}_k} = \underline{K}_{T,k}$ (see Equation (6)) and reorganizing to give

$$\frac{df}{d\underline{x}} = \frac{\partial f}{\partial \underline{x}} + \left(\frac{\partial f}{\partial \underline{u}_k} + \lambda_k^T \underline{K}_{T,k} \right) \frac{d\underline{u}_k}{d\underline{x}} + \lambda_k^T \frac{\partial \underline{R}_k}{\partial \underline{x}}, \tag{35}$$

the Lagrangian multipliers λ_k^T are now chosen to eliminate the implicit sensitivity of the second term (and specifically $\frac{d\underline{u}_k}{d\underline{x}}$), by solving the so-called adjoint equation

$$\lambda_k^T \underline{K}_{T,k} = - \frac{\partial f}{\partial \underline{u}_k}, \tag{36}$$

where $\underline{K}_{T,k}$ can be extracted from the finite-element analysis so that we can solve for λ if we have $\frac{\partial f}{\partial \underline{u}_k}$.

We can then simplify the terms of sensitivities in Equation (35), revealing the general sensitivity formulation

$$\frac{df}{d\underline{x}} = \frac{\partial f}{\partial \underline{x}} + \lambda_k^T \frac{\partial \underline{R}_k}{\partial \underline{x}}, \tag{37}$$

where the partial derivative of the residual forces with respect to the design variables $\frac{\partial \underline{R}_k}{\partial \underline{x}}$ is calculated analytically in the implemented FE code.

It should be further noted that filter and projection methods as well as the energy interpolation approach are used for topology optimization in this work. Therefore, to obtain sensitivities with respect to the design variables \underline{x} , a chain rule approach has to be applied to the general sensitivity Equation (37) in order to account for Equations (10)–(15) Wang et al. [47]. This is giving the terms

$$\frac{\partial f}{\partial \underline{x}} = \left(\frac{\partial f}{\partial \underline{\bar{x}}} + \frac{\partial f}{\partial \gamma} \frac{\partial \gamma}{\partial \underline{\bar{x}}} \right) \frac{\partial \underline{\bar{x}}}{\partial \underline{x}} \frac{\partial \underline{\bar{x}}}{\partial \underline{x}}, \tag{38}$$

$$\frac{\partial \underline{R}_k}{\partial \underline{x}} = \left(\frac{\partial \underline{R}_k}{\partial \underline{\bar{x}}} + \frac{\partial \underline{R}_k}{\partial \gamma} \frac{\partial \gamma}{\partial \underline{\bar{x}}} \right) \frac{\partial \underline{\bar{x}}}{\partial \underline{x}} \frac{\partial \underline{\bar{x}}}{\partial \underline{x}}, \tag{39}$$

where $\frac{\partial f}{\partial \gamma}$ is zero, but $\frac{\partial \underline{R}_k}{\partial \gamma}$ is nonzero (cf. Equation (14)).

In the following, we concentrate on the specific values and develop $\frac{\partial f}{\partial \underline{\bar{x}}}$ as well as the Lagrangian multipliers λ_k^T (via $\frac{\partial f}{\partial \underline{u}}$) for each of the functionals of the optimization problems.

2.3.1. Maximum Displacement Objective Sensitivity

The function of interest is the maximum displacement objective f_u , given in Equation (16). The partial derivative with respect to the element densities is

$$\frac{\partial f_u}{\partial \underline{\bar{x}}} = \underline{0}^T. \tag{40}$$

The Lagrangian multipliers are solved in this case via Equation (36) with the relation

$$\frac{\partial f_u}{\partial \underline{u}} = -\underline{L}^\top. \tag{41}$$

We then solve the following equation for λ :

$$\underline{K}_T \lambda = \underline{L}. \tag{42}$$

Plugging in the respective values in Equation (37) gives the derivative of the maximum displacement objective

$$\frac{df_u}{d\bar{x}} = \lambda^\top \frac{\partial R_k}{\partial \bar{x}}. \tag{43}$$

2.3.2. Path Generation Objective Sensitivity

Using the results from above, we can derive the sensitivities for the path-generation objective function in Equation (17). Therefore, we take the total derivative

$$\frac{df_{\text{path}}}{d\bar{x}} = \sum_{i=0}^n \alpha_i \sum_{j=1}^m \sum_{k=1}^l 2 \underbrace{\left(\frac{d(L_k^\top \underline{u}_{i,j})}{d\bar{x}} \right)}_{\hat{=} -\frac{df_u}{d\bar{x}}} (L_k^\top \underline{u}_{i,j} - u_{k,j}^*), \tag{44}$$

recognizing from above that the sensitivity $\frac{df_u}{d\bar{x}}$ can be expressed by Equation (43). Using this relation in Equation (44), we derive the following expression

$$\frac{df_{\text{path}}}{d\bar{x}} = \sum_{i=0}^n \alpha_i \sum_{j=1}^m \sum_{k=1}^l -2\lambda_{k,i,j}^\top \frac{\partial R_{i,j}}{\partial \bar{x}} (L_k^\top \underline{u}_{i,j} - u_{k,j}^*). \tag{45}$$

In order to obtain the sensitivity for each precision point j and load case i , the corresponding tangent stiffness matrix $\underline{K}_{T,i,j}$ and residual vector $\underline{R}_{i,j}$ are stored in memory. The Lagrange multipliers $\lambda_{k,i,j}$ are solved for inserting the corresponding values $\underline{K}_{T,i,j}$ and \underline{L}_k into Equation (42).

2.3.3. Volume Constraint Sensitivity

For the sensitivity of the volume constraint function in Equation (19), a direct derivation is used. This is defined as

$$\frac{dg_V}{d\bar{x}_i} = \frac{V_i}{\varphi_{\text{allow}} V_{\text{tot}}}. \tag{46}$$

2.3.4. Stress Constraint Sensitivity

The sensitivities of the stress constraint function defined in Equation (27) are also derived by the same approach as in Section 2.3.1. Starting with the partial derivative of the stress constraint function

$$\frac{\partial g_\sigma}{\partial \bar{x}} = \frac{1}{\sigma_{\text{allow}}} \frac{\partial \hat{\sigma}_p}{\partial \bar{x}}, \tag{47}$$

where

$$\frac{\partial \hat{\sigma}_p}{\partial \bar{x}_l} = c \left(\sum_i V_i \tilde{\sigma}_i^p \right)^{\frac{1-p}{p}} V_l \tilde{\sigma}_l^{p-1} q \bar{x}_l^{q-1} \sigma_{M,l}, \tag{48}$$

with element index l . The partial derivative with respect to the state variables \underline{u} is

$$\frac{\partial g_\sigma}{\partial \underline{u}} = \frac{1}{\sigma_{\text{allow}}} \frac{\partial \hat{\sigma}_p}{\partial \underline{u}}. \tag{49}$$

Using this relation we write the linear adjoint system according to Equation (36) as

$$\underline{\underline{K}}_T \lambda = - \frac{\partial g_\sigma}{\partial \underline{u}}^\top. \tag{50}$$

For solving this equation for the Lagrange multipliers, we need $\frac{\partial \hat{\sigma}_p}{\partial \underline{u}}$, which is defined by element via

$$\frac{\partial \hat{\sigma}_p}{\partial \underline{u}_l} = c \left(\sum_i V_i \tilde{\sigma}_i^p \right)^{\frac{1-p}{p}} V_l \tilde{\sigma}_l^{p-1} \tilde{x}_l^q \frac{1}{\sigma_{M,l}} \underline{\underline{\sigma}}_{C,l}^\top \underline{\underline{A}} \frac{\partial \underline{\underline{\sigma}}_{C,l}}{\partial \underline{u}_l}. \tag{51}$$

The derivation of the sensitivities of the Cauchy stresses $\frac{\partial \underline{\underline{\sigma}}_{C,l}}{\partial \underline{u}_l}$ is carried out by applying the product rule on Equation (7). The sensitivity with respect to the i th component of the l th elements nodal displacement vector \underline{u}_l is obtained as

$$\frac{\partial \underline{\underline{\sigma}}_{C,l}}{\partial u_{i,l}} = - \underbrace{\frac{1}{J_l^2} \frac{\partial J_l}{\partial u_{i,l}} \underline{\underline{F}}_l \underline{\underline{\sigma}}_{2PK,l} \underline{\underline{F}}_l^\top}_{(i)} + \underbrace{\frac{1}{J_l} \underline{\underline{F}}_l \frac{\partial \underline{\underline{\sigma}}_{2PK,l}}{\partial u_{i,l}} \underline{\underline{F}}_l^\top}_{(ii)} + \underbrace{\frac{1}{J_l} \left(\frac{\partial \underline{\underline{F}}_l}{\partial u_{i,l}} \underline{\underline{\sigma}}_{2PK,l} \underline{\underline{F}}_l^\top + \underline{\underline{F}}_l \underline{\underline{\sigma}}_{2PK,l} \left(\frac{\partial \underline{\underline{F}}_l}{\partial u_{i,l}} \right)^\top \right)}_{(iii)}. \tag{52}$$

Now generalizing Equation (52) for the entire element displacement vector \underline{u}_l and transferring it to Voigt notation, three core terms $\underline{\underline{T}}_1$, $\underline{\underline{T}}_2$ and $\underline{\underline{T}}_3$ can be distinguished, corresponding to (i), (ii) and (iii), respectively,

$$\frac{\partial \underline{\underline{\sigma}}_C}{\partial \underline{u}_l} = \underline{\underline{T}}_1 + \underline{\underline{T}}_2 + \underline{\underline{T}}_3. \tag{53}$$

For the derivation of the term $\underline{\underline{T}}_1$, the only unknown is $\frac{\partial J_l}{\partial \underline{u}_l}$. It is obtained using the Voigt notation $\hat{\underline{\underline{C}}}$ of the inverse of the right Cauchy–Green tensor,

$$\hat{\underline{\underline{C}}} \triangleq \underline{\underline{C}}_l^{-1} = (\underline{\underline{F}}_l^\top \underline{\underline{F}}_l)^{-1}, \tag{54}$$

which results in

$$\frac{\partial J_l}{\partial \underline{u}_l} = J_l (\hat{\underline{\underline{C}}}_l)^\top \underline{\underline{F}}_l^\top \underline{\underline{B}}_{L,l}. \tag{55}$$

Moreover, the transformation to Voigt notation of the form

$$\underline{\underline{F}}_l \underline{\underline{\sigma}}_{2PK,l} \underline{\underline{F}}_l^\top \triangleq \underbrace{\begin{bmatrix} F_{11}^2 & F_{12}^2 & 2F_{11}F_{12} \\ F_{21}^2 & F_{22}^2 & 2F_{21}F_{22} \\ F_{11}F_{21} & F_{12}F_{22} & F_{11}F_{22} + F_{12}F_{21} \end{bmatrix}}_{\underline{\underline{Y}}_l} \underline{\underline{\sigma}}_{2PK,l}, \tag{56}$$

is used, leading to

$$\underline{\underline{T}}_1 = - \frac{1}{J_l} \underline{\underline{Y}}_l \underline{\underline{\sigma}}_{2PK,l} (\hat{\underline{\underline{C}}}_l)^\top \underline{\underline{F}}_l^\top \underline{\underline{B}}_{L,l}. \tag{57}$$

The Voigt expression in Equation (56) is also used to derive the second term $\underline{\underline{T}}_2$

$$\underline{\underline{T}}_2 = \frac{1}{J_l} \underline{\underline{Y}}_l \frac{\partial \underline{\underline{\sigma}}_{2PK,l}}{\partial \underline{\underline{\varepsilon}}_{GL,l}} \frac{\partial \underline{\underline{\varepsilon}}_{GL,l}}{\partial \underline{u}_l} = \frac{1}{J_l} \underline{\underline{Y}}_l \underline{\underline{C}}_{\underline{\underline{V}}K} \underline{\underline{F}}_l^\top \underline{\underline{B}}_{L,l}. \tag{58}$$

After further defining the matrix $\underline{\underline{X}}$,

$$\underline{\underline{X}}_l = \begin{bmatrix} X_{11} & X_{12} \\ X_{21} & X_{22} \end{bmatrix} = \underline{\underline{F}}_l \underline{\underline{\sigma}}_{2PK,l}, \tag{59}$$

the missing term \underline{T}_3 can be calculated from the components of \underline{X} as

$$\underline{T}_3 = \frac{1}{J_l} \begin{bmatrix} 2X_{11} & 0 & 2X_{12} & 0 \\ 0 & 2X_{22} & 0 & 2X_{21} \\ X_{21} & X_{12} & X_{22} & X_{11} \end{bmatrix} \underline{B}_{L,l}. \tag{60}$$

We finally obtain the total derivative of the stress constraint function with respect to the design variables by plugging in the values into the following equation:

$$\frac{dg_\sigma}{d\bar{x}} = \frac{\partial g_\sigma}{\partial \bar{x}} + \lambda^T \frac{\partial R}{\partial \bar{x}}. \tag{61}$$

2.3.5. Sensitivity Analysis for Multiresolution Topology Optimization

The sensitivity equations derived in the prior sections for the objective functions can be used analogously for multiresolution topology optimization. The only difference is that more design variables than finite-elements are used. This has an impact on the calculation of the terms $\frac{\partial R_k}{\partial \bar{x}}$ (see Equation (37)), because \bar{x} is of higher dimension. The adjoint Equation (36) for the objective function sensitivities remains unchanged.

In addition, the sensitivities of the volume constraint function in Equation (46) remain unchanged.

The sensitivity functions of the stress constraint Equation (27) are changed if multiresolution topology optimization is used. Due to the use of the stress values $\underline{\sigma}_{C,i,j}$ at each integration point (or subelement) j , the p-norm function changes to Equation (30). This affects the partial derivative of the normalized p-norm which for the MTOP approach is written as

$$\frac{\partial \hat{\sigma}_p}{\partial \bar{x}_l} = c \left(\sum_i \sum_j V_{i,j} \tilde{\sigma}_{i,j}^p \right)^{\frac{1-p}{p}} V_l \tilde{\sigma}_l^{p-1} q \bar{x}_l^{q-1} \sigma_{M,l}. \tag{62}$$

The partial derivative of the p-norm with respect to the element displacement vector \underline{u} previously introduced in Equation (51) must be adapted to the MTOP approach. Whereas the displacement vector \underline{u} is defined for the displacement elements and hence remains the same, the stress of each individual density subelement $\underline{\sigma}_{C,i,j}$ must be considered. The sensitivity function for stress in MTOP is

$$\frac{\partial \hat{\sigma}_p}{\partial \underline{u}_l} = \sum_j c \left(\sum_i \sum_j V_{i,j} \tilde{\sigma}_{i,j}^p \right)^{\frac{1-p}{p}} V_{l,j} \tilde{\sigma}_{l,j}^{p-1} \bar{x}_{l,j}^q \frac{1}{\sigma_{M,l,j}} \underline{\sigma}_{C,l,j}^T \underline{A} \frac{\partial \underline{\sigma}_{C,l,j}}{\partial \underline{u}_l}. \tag{63}$$

3. Numerical Examples

In the following, results for the two different objective functions are presented. First, the importance of nonlinear analysis and the effect of the introduced stress-constrained formulation are shown. The results of a maximum-displacement gripper example are compared. After giving this motivation for nonlinear analysis, we show the effect of stress constraints on a path-generating mechanism. Multiresolution topology optimization results are shown in comparison to the standard topology optimization solutions. The ability of the proposed methodology for use in large-scale examples is shown with the optimization of a compliant mechanism rib structure for a droop-nose morphing wing concept. The same material properties, parameters for the structural–mechanical analysis and optimization settings are used throughout.

3.1. Material and Constitutive Law

In the following studies, we use a generic thermoplastic polymer of the type polyether ether ketone (PEEK). PEEK can be used in both more traditional, subtractive manufacturing techniques as well as with additive manufacturing via fused filament fabrication (FFF) and

selective laser sintering (SLS). The latter two methods, also known as three-dimensional printing, allow for the full utilization of the geometries found via topology optimization.

For the following design problems, we use a linear-elastic material model for PEEK. The material properties used can be found in Table 1. As compliant mechanisms are intended to be cyclic loaded, a knockdown factor of two from limit stress has been used for determining the allowable stress for the stress constraint optimization.

Table 1. Material parameters for a generic polyether ether ketone (PEEK).

Parameter	Symbol	Value	Units
Young’s modulus	E	4232	MPa
Poisson’s ratio	ν	0.36	–
Limit stress	σ_{limit}	100	MPa
Max allowable stress	σ_{allow}	50	MPa

3.2. Numerical Example—Maximum Displacement Mechanism Design

We define the optimization problem for the maximization of a mechanism’s output displacement u_{out} (problem type I) as

$$\begin{aligned}
 & \min_{\underline{x}} \{f_u\} \\
 & \text{where } f_u(\underline{x}) = -\underline{L}^T \underline{u}(\underline{x}) \\
 & \text{subject to } g_V(\underline{x}) = \frac{\varphi(\underline{x})}{\varphi_{\text{allow}}} - 1 \leq 0, \\
 & \qquad \qquad g_\sigma(\underline{x}) = \frac{\hat{\sigma}_{pk}(\underline{x})}{\sigma_{\text{allow}}} - 1 \leq 0 \\
 & \qquad \qquad 0 \leq x_i \leq 1 \\
 & \text{governed by } \underline{R} = \underline{P}_{\text{int}} - \underline{P}_{\text{ext}} = 0
 \end{aligned} \tag{64}$$

where the output displacement function is defined by Equation (16). The example for this optimization problem is a gripping mechanism illustrated in Figure 2. Within a rectangular domain, a topology is sought that transfers an input displacement caused by the input force P_{in} into a maximum output displacement u_{out} at the right-hand side of the domain. Springs k_{in} and k_{out} are added to simulate the stiffness of the input mechanism and output workpiece and hence to pose a minimum load transferring requirement on the mechanism. The gray area represents the designable domain, whereas black and white areas represent non-designable solid and void, respectively. All non-designable solid regions have a height of 0.05 h. The corresponding parameter values for the optimization problem defined by Equation (64) and Figure 2 are listed in Tables 1 and 2. In order to solve the optimization problem, the design space is discretized with bilinear quadrilateral finite elements and the symmetry of the design problem is exploited. The integrals for the residuum and stiffness are approximated by Gauss integration using four Gauss points per element.

Results for linear and nonlinear FEA, both with and without stress constraints are shown in Figure 3. Four different topologies can be observed. It should be noted that the results shown are the results of the topology optimization without smoothing. To the left, solutions with volume constraints are illustrated and to the right, stress constraints are additionally applied. For all the results, the volume constraint is satisfied. For the problem formulation with only a volume constraint, the maximum stresses exceed the limit stress, which would lead to failure of this mechanisms at its first actuation. This, as well as the occurrence of nonphysical one node connected hinges in those solutions, excludes practical realization of the mechanisms. The stress constraints successfully alleviate both of the mentioned problems, by eliminating high stress localized hinge regions from the topologies and substituting them with so-called distributed compliance hinges. Hence, the maximum occurring stress level can be lowered to the prescribed limit.

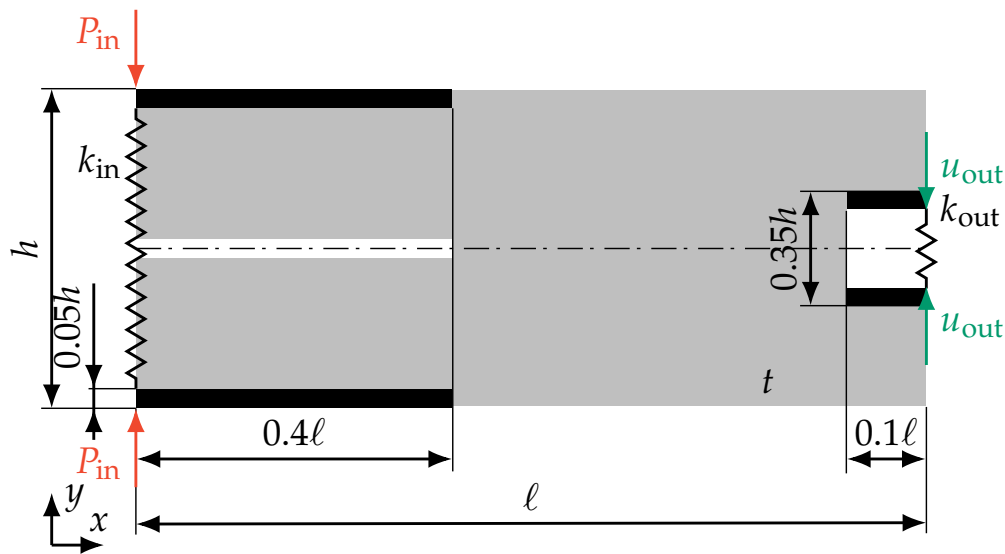


Figure 2. Example definition scheme for maximum output displacement gripper (gray: design space, black: non-design space of solid material, white: non-design space of voids).

Table 2. Parameters specific for maximum displacement example.

Parameter	Symbol	Value	Units
Minimum Young's modulus	E_{\min}	4.232×10^{-6}	MPa
Input force	P_{in}	50	N
Length	ℓ	200	mm
Height	h	80	mm
Thickness	t	5	mm
Input stiffness	k_{in}	1.5	N/mm
Output stiffness	k_{out}	4	N/mm
Filter radius	r_{\min}	4.7	mm
Volume fraction	φ_{allow}	0.3	–

Comparing the linear to the nonlinear results, also notable differences in the topology can be observed. Commonality is seen though in the large rigid regions, which are dosed based on the value of the volume fraction constraint. The differences become especially evident by looking at the mechanisms performance in terms of output displacement and maximum stress level. Those result values are listed for the different solution topologies in Table 3, where also a nonlinear analysis is performed on the linear optimization results. As shown by [14] it can be seen that, due to the neglected nonlinear effects the performance of the linearly obtained mechanism topologies is drastically overestimated. This means not only that overly high values are obtained for the output displacements, but also that at the same time the actual stress level is underestimated. Looking at topology in Table 3b this important impact of nonlinear effects on the results becomes evident. Here, for linear theory, the stress constraint could successfully limit the stresses, but taking nonlinear effects into account stress levels still exceed by far the prescribed limit of σ_{allow} . In contrast, topologies in Table 3c,d were found considering the nonlinearities during optimization and therefore lead to a better mechanism performance.

As prior to manufacturing, the results are commonly smoothed, e.g., in order to eliminate jagged edges from the mechanisms, slight changes in the stress field and objective function values will be the consequence. The effect of smoothing the results obtained here is investigated in Figure 4, where the stress field of the smoothed topology for the nonlinear stress constrained solution in Figure 3d is shown. A Laplacian filter was used to generate the smoothed result, which then was remeshed resulting in a nonregular FE mesh. It can be seen that no significant changes in the stress field occur. In Table 3, the maximum

stress and the objective function value for the smoothed solution are shown. Due to slight geometrical changes and the lack of low stiffness void elements the objective function was improved by 5%, meanwhile the maximum stress increased by 4%. It can be stated that as long as geometrical changes due to smoothing of the results topologies are marginal, sufficiently accurate values are obtained by the introduced method.

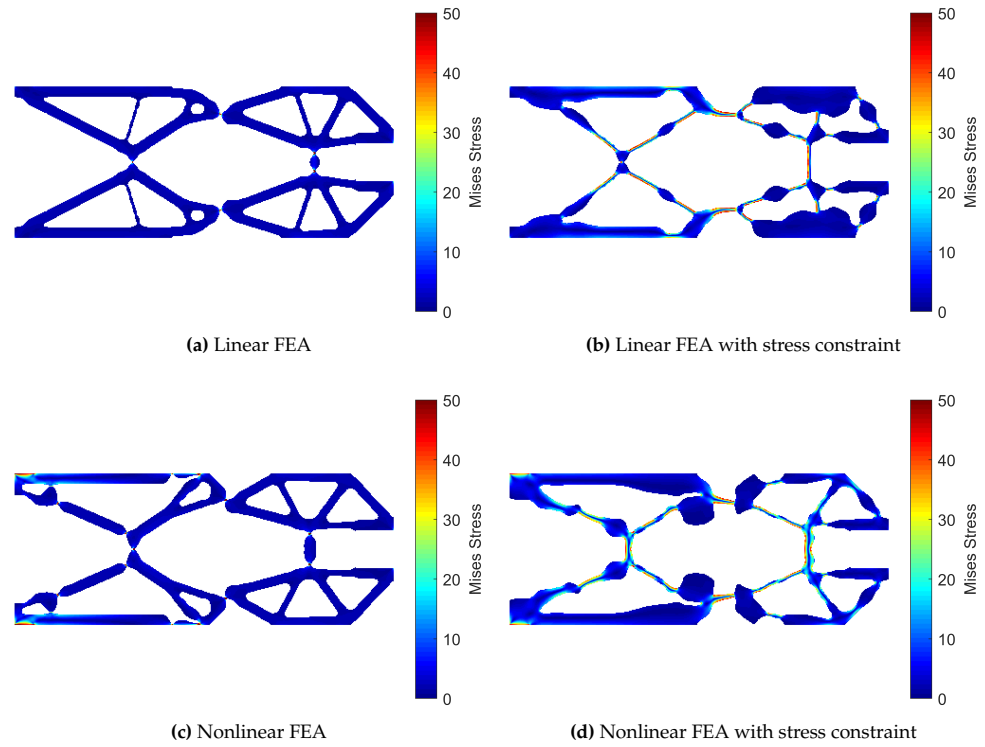


Figure 3. Comparison of topology optimization results for the maximum output displacement gripper example (400×80 elements).

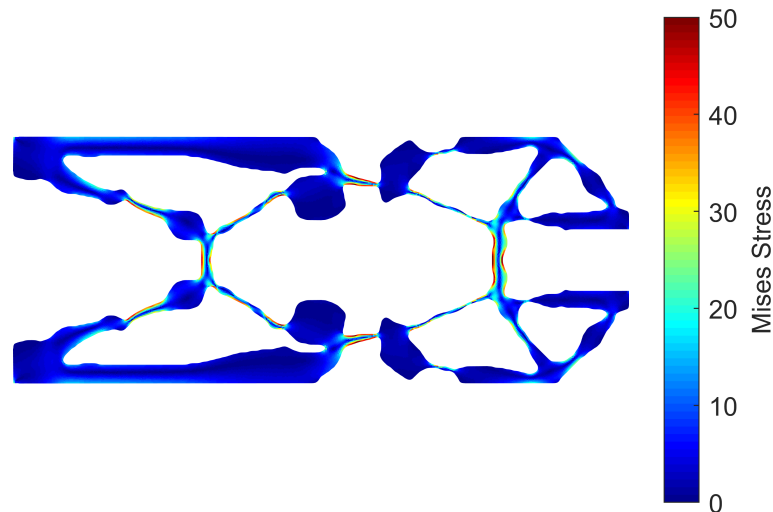


Figure 4. Stress field for gripper result based on Figure 3d with smoothed boundary (12,451 solid elements and 0 void elements).

Table 3. Output displacement and maximum stress values for the gripper mechanism topologies in Figures 3 and 4.

Solution Topology	Validation Analysis Type	u_{out} [mm]	$\max \bar{\sigma}$ [MPa]
a (Figure 3a)	linear	9.76	528.28
	nonlinear	7.23	624.65
b (Figure 3b)	linear	7.55	49.37
	nonlinear	5.53	173.74
c (Figure 3c)	nonlinear	7.84	571.28
d (Figure 3d)	nonlinear	4.27	49.95
e (Figure 4)	nonlinear	4.50	51.99

3.3. Numerical Example—Path-Generation Mechanism Design

We introduce the novel case of the addition of stress constraints to the topology optimization of path-generating compliant mechanisms and show results for a generic example mechanism. Moreover, we apply the introduced extension of multiresolution topology optimization to stress constrained problems to this example and compare the results (problem type II). The complete optimization problem is formulated as

$$\begin{aligned}
 & \min_{\underline{x}} \{f_{\text{path}}\} \\
 \text{where } & f_{\text{path}}(\underline{x}) = \sum_{i=0}^n \alpha_i \sum_{j=1}^m \sum_{k=1}^l (\underline{L}_k^T \underline{u}_{i,j} - u_{k,j}^*)^2 \\
 \text{subject to } & g_V(\underline{x}) = \frac{\varphi(\underline{x})}{\varphi_{\text{allow}}} - 1 \leq 0 \\
 & g_\sigma(\underline{x}) = \frac{\hat{\sigma}_{p,k}(\underline{x})}{\sigma_{\text{allow}}} - 1 \leq 0 \\
 & 0 \leq x_i \leq 1 \\
 \text{governed by } & \underline{R} = \underline{P}_{\text{int}} - \underline{P}_{\text{ext}} = \underline{0}.
 \end{aligned} \tag{65}$$

Due to multiple load cases and deformation states considered in the path-generation approach, stress constraints can be considered for each case. The focus in this work is the general applicability of the stress constrained formulation to this problem type. Therefore, only the stress state in the last precision point for the zero counter load case $j = 3$ is constrained.

An example for a path-generation mechanism problem is defined in Figure 5, where the gray area again represents the available design space and the black areas represent prescribed solid regions. A mechanism is to be found that most closely transforms an input motion u_{in} in positive x -direction into a circular output motion u_{out} as prescribed in Table 4. This prescribed output path must be followed under each of the load cases specified in Table 5. For this example the input node is allowed to deform freely in y -direction. The parameters t , E_{min} and the filter radius r_{min} are selected according to Table 2 equal to the prior example. The domain length is $l = 100$ mm and a volume fraction constraint of $\varphi_{\text{allow}} = 0.2$ is selected. Bilinear quadrilateral finite elements including four Gauss integration points and the linear elastic material defined by Table 1 are used for the structural analysis (same as previous example).

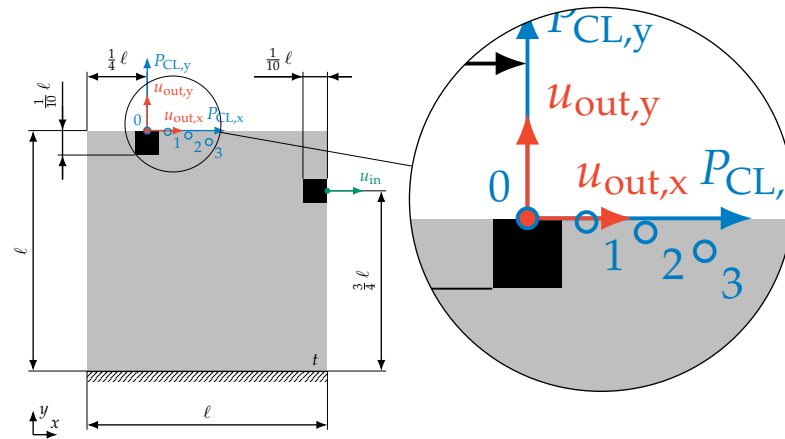


Figure 5. Example definition scheme for an output path generating compliant mechanism (gray: design space, black: non-design space of solid material).

Table 4. Precision points for the path-generation example.

Precision Point j	u_{in} [mm]	$u_{out,x}^*$ [mm]	$u_{out,y}^*$ [mm]
1	1.5	3	-0.18
2	3	6	-0.73
3	4.5	9	-1.67

Table 5. Load cases for the path generation example.

Load Case i	α [-]	$P_{CL,x}$ [N]	$P_{CL,y}$ [N]
0	1	0	0
1	0.1	40	40
2	0.1	-40	40

Figure 6 shows the results for the output path-generation mechanism example. Above, the solution was obtained by volume constrained topology optimization. Below, a stress constraint was additionally applied. From top to bottom, the solutions' deformation states and stress distributions for the different precision points j are shown. The corresponding load case is the case of no counter load. For the depicted case, both results approximate the prescribed path closely. Moreover, it is observed that the stress constraints again successfully reduce the maximum stress level. This is achieved at the cost of a slightly higher objective function value of $f = 0.224 \text{ mm}^2$ compared to $f = 0.155 \text{ mm}^2$ for the volume constrained solution. Looking closer to the stress fields, it can be further seen that the maximum stress in the volume constrained topology exceeds the material strength for each precision point. In contrast, the maximum stress of the stress constraint reaches the prescribed threshold value only in the last precision point, where also the largest deformations occur.

The example is also demonstrated with the stress field of a smoothed solution topology. Therefore, the stress constrained solution in Figure 6 is smoothed by Laplacian smoothing and remeshed. Figure 7 shows the stress field on the deformed geometry for the 3rd precision point. The maximum stress of the smoothed geometry increases by 4% compared to the solution in Figure 6f. Again also slight changes in the output displacements are observed.

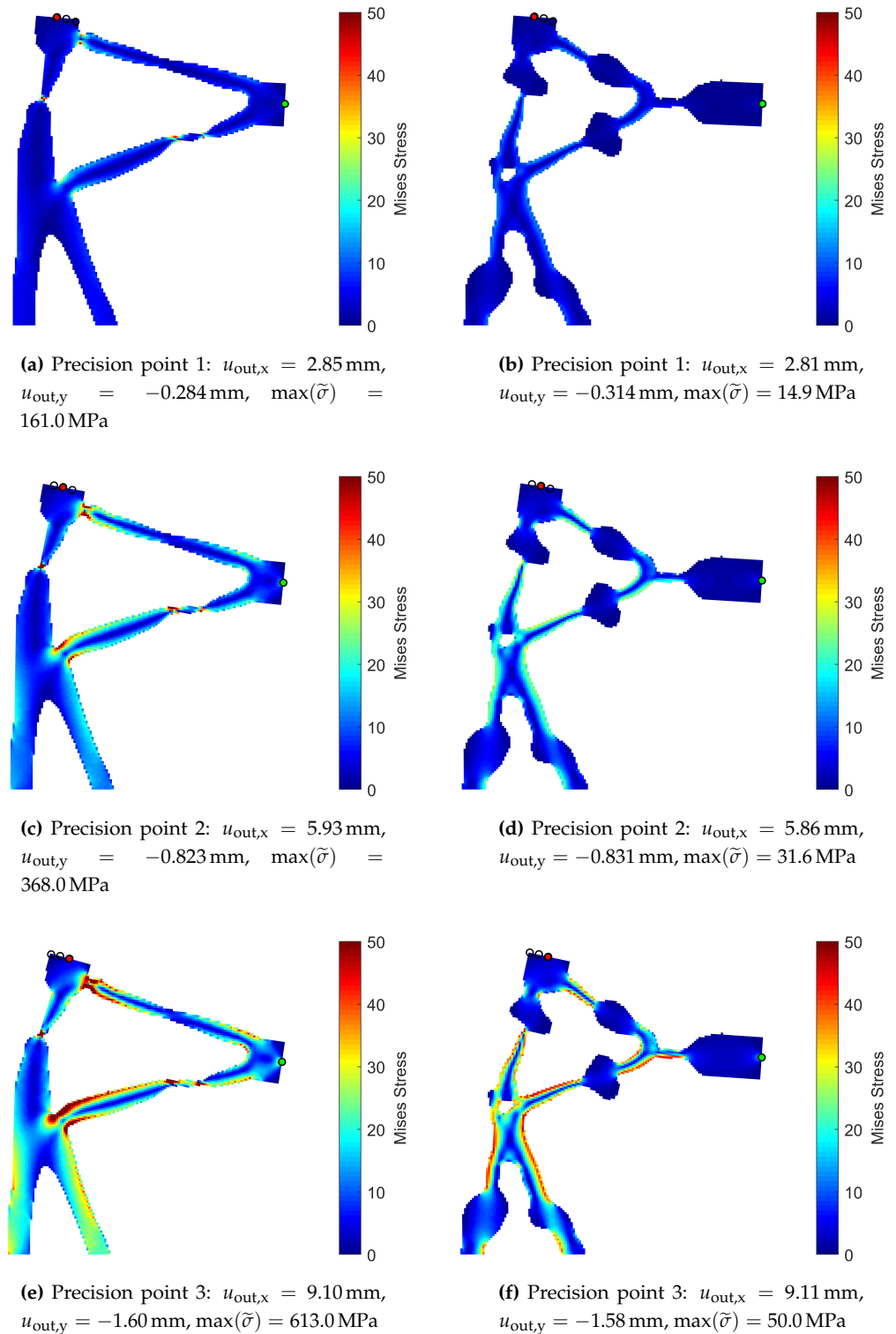


Figure 6. Comparison of the path generating example mechanism results for the three precision points in the load case $i = 0$ with 150×150 elements, volume constrained on the left, stress and volume constrained on the right.

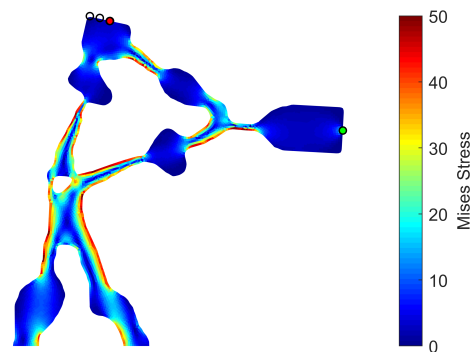


Figure 7. Path generating example mechanism topology with smoothed boundary based on Figure 6f: $u_{out,x} = 9.09$ mm, $u_{out,y} = -1.65$ mm, $\max(\bar{\sigma}) = 53.7$ MPa (5283 solid elements/0 void elements).

In Figure 8, results obtained by the multiresolution topology optimization method on a coarser 75×75 FE mesh are shown and compared to the results of Figure 6. The density meshes are equally sized (150×150) for both methods used. The coarser FE mesh is chosen in order to demonstrate the ability of the MTOP approach to find high resolution results based on relatively low resolution FE discretization. Results for the volume constrained as well as for the additionally stress constrained problem solutions could be successfully generated by the MTOP method. Comparing the volume constrained solutions in Figure 8a,c it can be seen that for the multiresolution topology optimization lower stress values occur. The reason for this is a less-precise stress modeling due to the larger size of the FE-elements. Due to the different FE discretization, also a different local minimum is found for the multiresolution topology optimization in Figure 8c. In Figure 8b,d, the stress and volume constrained results are compared. For both results the stress constraint successfully reduced the maximum stress to the threshold value. The MTOP result in Figure 8d is influenced by the underestimation of the stress field, hence thicker flexible joint regions are allowed. Computational time could be reduced by the MTOP method on the same desktop PC (Intel Core i7-7500U CPU @ 2.70GHz, 16GB DDR4) by approx. 75% for both examples.

The results in Figure 8 show that the introduced formulation of the multiresolution topology optimization method can be effectively used for stress constrained problems. Nevertheless, it has to be considered that the minimum size of the FE mesh has to be chosen sufficiently small in order to ensure a correct stress modeling.

The output paths and the prescribed precision points for the various results of the path generation mechanism example are plotted in Figure 9. It can be seen that the output path of each result is a clearly nonlinear curve, which approximates the precision points. The impact of the smoothing on the output path can be clearly observed, leading to a higher discrepancy between output path and precision points. This shows that results for path-generation examples are more sensitive to geometrical deviations. Therefore, the introduction of manufacturing constraints to this type of problems would be a natural extension.

3.4. Engineering Example—Morphing Wing Design

The numerical results culminate with a practical example for the application of the introduced methods. In this case, the internal structure (compliant mechanism) for the deformation of the morphing leading edge of a sailplane wing is designed. The airfoil and wing planform for the morphing wing concept is designed by [54,55] and its elastic wing shell is described by [56]. As sailplanes have a large operation envelope, the ability to morph the wing results in drastic performance gains. Figure 10 shows a schematic problem definition for a compliant mechanism rib to be used in a droop-nose morphing wing concept. A compliant mechanism that displaces an output node on the outer leading edge contour in a predefined position u_{out} (problem type II) is sought. Combining multiple

mechanisms of this type along the leading edge contour allows the wing to be morphed accurately to a target airfoil. The mechanisms defining an airfoil are stacked together in span direction and connected by a belt along the leading edge contour. By this means, a single rib is formed, which can be bonded to the wings shell. In span direction of the wing multiple of these stacked ribs are used, considering the changing airfoils along the wing. The optimization problem defined in Equation (65) is used to synthesize such mechanisms.

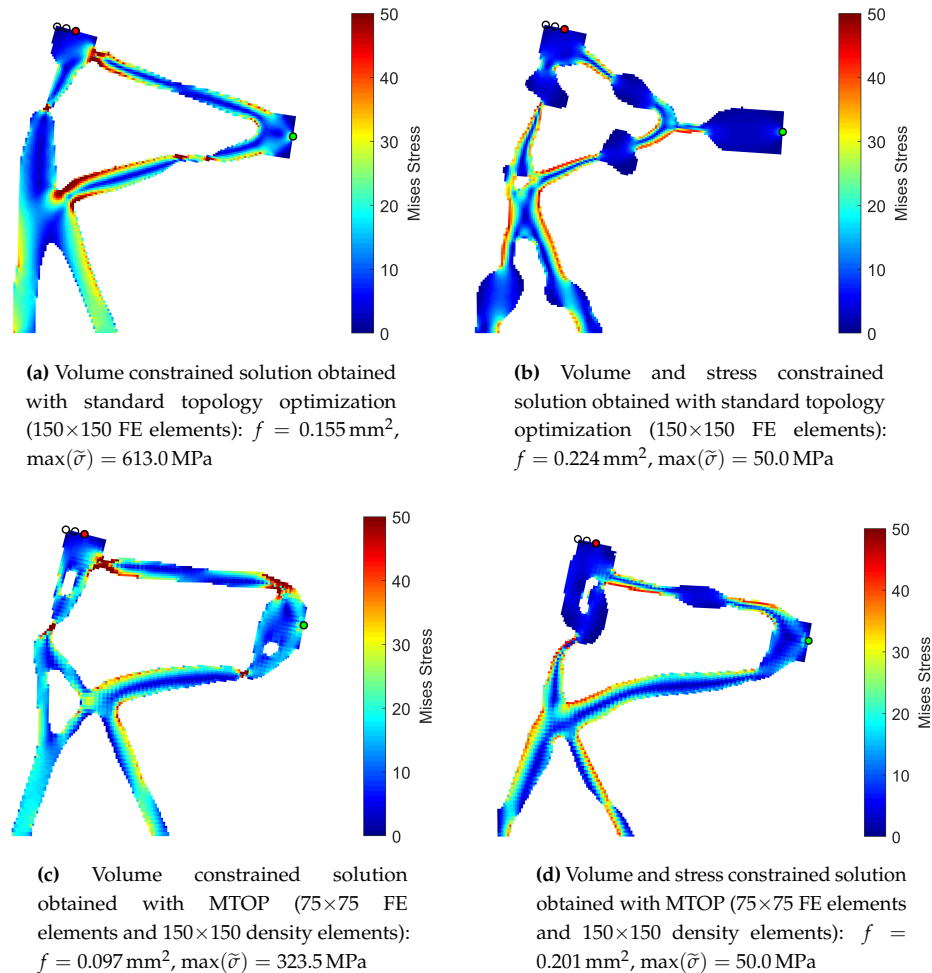


Figure 8. Path generating example solutions with and without multiresolution topology optimization.

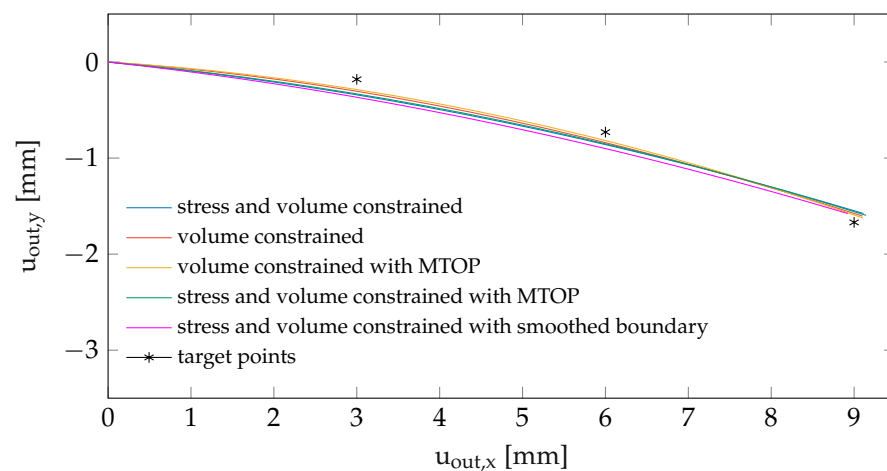


Figure 9. Output paths for path generation mechanism example solutions in Figures 6 and 7.

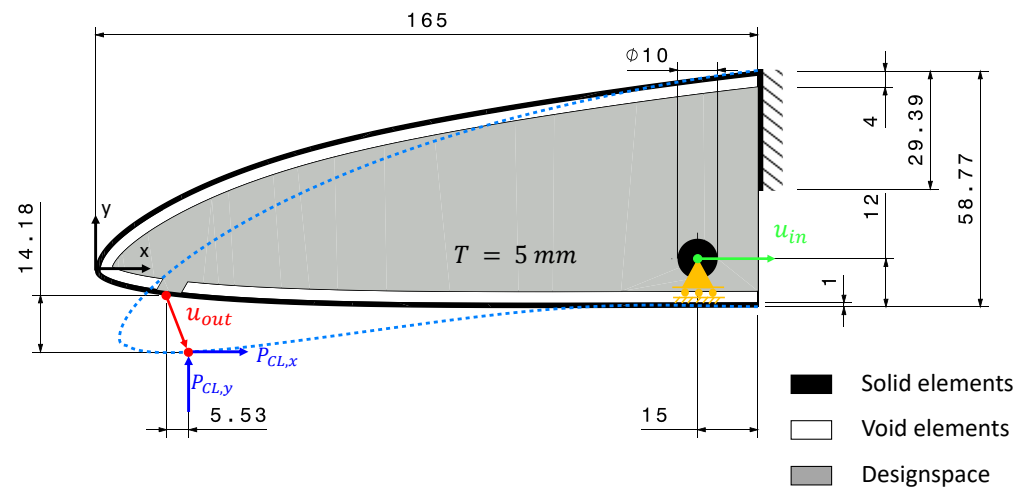


Figure 10. Problem definition for a compliant mechanism rib structure.

Table 6. Precision points for the rib example.

Precision Point j	u_{in} [mm]	$u_{out,x}^*$ [mm]	$u_{out,y}^*$ [mm]
1	4	5.53	-14.18

Table 7. Load cases for the rib example.

Load Case i	α [-]	$P_{CL,x}$ [N]	$P_{CL,y}$ [N]
0	1	0	0
1	0.1	14.2	32.8

In Figure 10, the gray area represents the designable domain, whereas black and white areas represents non-designable solid or void, respectively. To the upper right, fixed supports represent an adhesive fixation of the mechanism to the wings spar. The mechanism is activated by the application of a positive x-displacement u_{in} at the input node, which is guided by a support in the y-direction (shown in yellow). The design space is discretized by bilinear quadrilateral finite elements with four Gauss integration points. Material and optimization parameters are used according to the path generation example shown in advance. Only one precision point prescribes the target position of the output node in the activated, i.e., morphed state (see Table 6). The counter load cases are set according to Table 7 simulating aerodynamic loads on the mechanism acting against the direction of deformation.

In Figure 11, the deformed results for the compliant mechanism rib are compared for the various optimization methods used. In Figure 11a, the problem was solved without consideration of stress constraints. It can be observed that a low objective function value is reached as this design provides a good approximation of the target displacement. On the other hand, a practical application of the mechanism is excluded due to the high stresses in the flexible hinges connecting the mechanism to the support. These stresses would lead to failure of the mechanism. In Figure 11b, stress constraints were also considered. The stresses are reduced to the admissible level at the cost of a slightly higher deviation from the exact target displacement. A mechanism suitable for practical application could be obtained.

Figure 11c,d show respectively the results for the volume-constrained as well as the volume- and stress-constrained rib mechanism obtained by the MTOP method. Therefore, the same FE mesh is used as in Figure 11a,b but with a four times higher resolution of the density mesh. By this means, similar topologies are obtained as for the standard topology optimization in Figure 11a,b but at a higher resolution. The obtained results are hence

less discrete, smoother and hence closer to the manufactured geometry. In Figure 12, a 3D printed demonstrator of a combination of various compliant mechanism ribs obtained by the introduced method is shown.

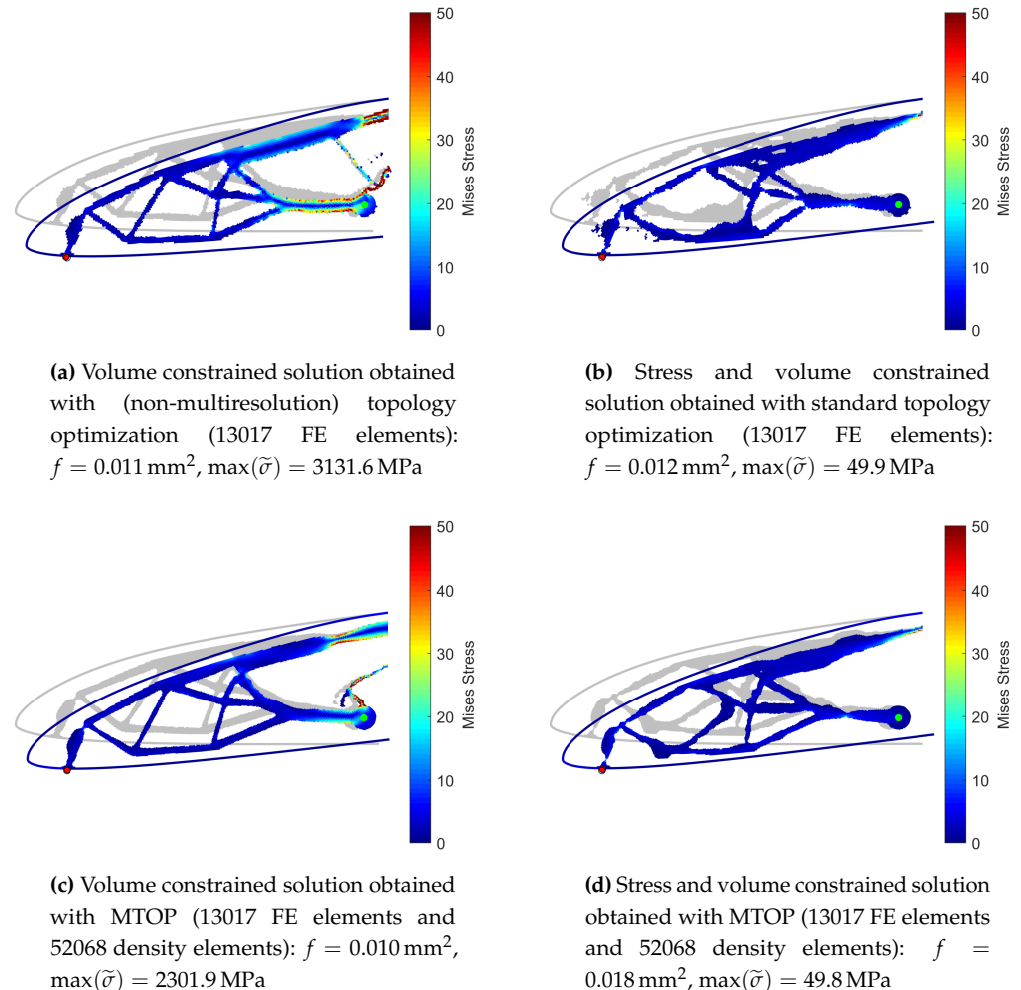


Figure 11. Comparison of solutions for the compliant mechanism rib example.



Figure 12. Morphing wing demonstrator based on topology optimization results showing undeformed and deformed states.

4. Conclusions

The results of this work clearly demonstrate the necessity of both nonlinear finite-element analysis and stress constraints in the topology optimization of compliant mechanisms. To achieve this, multiresolution stress-constrained topology optimization with nonlinear finite-element analysis has been implemented for maximum displacement and path-generation mechanisms. Without stress constraints, the resulting topologies of the introduced problems exhibit stresses well beyond the limits, especially because of the formation of one-node hinges. Through proper choice of stress limits in concert with filtering parameters, designs were found that can function without violation of strength limits. As large displacements and rotations are actually desired with this design problem,

nonlinear finite-element analysis is necessary to properly represent deformations, strains and stresses.

These two aspects represent a challenge to its implementation, not only for the primal analysis but also in the calculation of the sensitivities. Based on a total Lagrangian formulation, we have derived the sensitivities of the objective and constraint functions via an adjoint methodology.

The introduced topology optimization methodology is applied to two numerical examples with different objective functions: maximum displacement and path-following designs. For the former, we clearly show the different resulting optimal topologies from

- linear finite-element analysis with volume constraint;
- linear finite-element analysis with volume and stress constraints;
- nonlinear finite-element analysis with volume constraint;
- nonlinear finite-element analysis with volume and stress constraints.

Nonlinear analysis is necessary for the path-following design as linear analysis will not follow a curved path. By applying stress constraints to the path-generation design problem, an approach for the synthesis of fatigue resistant prescribed path following mechanisms is shown. Moreover, a novel methodology for the consideration of stress constraints in multiresolution topology optimization is introduced and applied to the examples for the path-generation mechanisms. As a conclusion, an engineering example of a mechanism designed for a morphing wing application is discussed, showing a possible practical application of the introduced methods.

Future work will explore the reduction in the large amount of iterations (ca. 250) to increase computational efficiency, the extension of the path generation problem formulation to multiple output nodes as well as the expansion to a geometrically robust formulation. Other challenges include the high number of parameter values in the optimization formulation that have a large influence on the resulting topology and convergence. More specific knowledge about the influence and mutual interference of these parameters must be gained. Furthermore, the issue of unstable behavior in void elements and resulting ill-convergence is still not fully resolved for all types of problems. Although the interpolation scheme based on Wang et al. [47] and applied in this work significantly improved the stability of the finite-element analysis, instabilities still occur in intermediate density elements. This problem could be resolved by a thorough study of the interpolation parameters of Equation (15). However, there are also promising recent approaches based on contact modeling theory, as shown by Bluhm et al. [57], where the material strain energy function has been augmented with an energy associated with higher order strains. This approach penalizes only mesh bending and warping distortion in high strained low density elements and not homogeneous deformation states. It also introduces self-contact modeling with low additional computational cost, paving the way for the synthesis of compliant mechanisms making use of self-contact. However, as this is very recent research, this was not implemented into the current work yet. Despite these challenges, we have shown promising results for compliant structures using nonlinear finite-element analysis.

Author Contributions: J.R.: conceptualization, data curation, formal analysis, investigation, methodology, software, visualization, writing—original draft preparation, writing—reviewing and editing. E.W.: conceptualization, funding acquisition, methodology, project administration, supervision, writing—original draft preparation, writing—reviewing and editing. J.A.: conceptualization, funding acquisition, methodology, project administration, supervision, writing—reviewing and editing. All authors have read and agreed to the published version of the manuscript.

Funding: This work was conducted within the projects LightMech3D—Synthesis of lightweight compliant mechanisms with topology optimization for three-dimensional printing and MILAN—Morphing wings for sailplanes. The former is funded by the Free University of Bozen-Bolzano (TN2097), while the latter is funded by the German Federal Ministry for Economic Affairs and Energy under the grant of the German Federal Aviation Research Program (Luftfahrtforschungsprogramm,

LuFo) V-3. The publication of this work was supported by the Open Access Publishing Fund provided by the Free University of Bozen-Bolzano.

Conflicts of Interest: The authors declare no conflict of interest.

References

- Howell, L. *Compliant Mechanisms*; A Wiley-Interscience Publication; Wiley: Hoboken, NJ, USA, 2001.
- Rojas, R.A.; Wehrle, E.; Vidoni, R. Optimal design for the passive control of vibration based limit cycles. *Shock Vib.* **2019**, *2019*, 1–11. [\[CrossRef\]](#)
- Michell, A. The limits of economy in frame-structures. *Philos. Mag.* **1904**, *8*, 589–597. [\[CrossRef\]](#)
- Bendsoe, M.P.; Kikuchi, N. Generating optimal topologies in structural design using a homogenization. *Comput. Methods Appl. Mech. Eng.* **1988**, *71*, 197–224. [\[CrossRef\]](#)
- Bendsoe, M.P. Optimal shape design as a material distribution problem. *Struct. Optim.* **1989**, *1*, 193–202. [\[CrossRef\]](#)
- Sigmund, O.; Petersson, J. Numerical instabilities in topology optimization: A survey on procedures dealing with checkerboards, mesh-dependencies and local minima. *Struct. Multidiscip. Optim.* **1998**. [\[CrossRef\]](#)
- Sigmund, O. On the usefulness of non-gradient approaches in topology optimization. *Struct. Multidiscip. Optim.* **2011**, *43*, 589–596. [\[CrossRef\]](#)
- Baumgartner, A.; Harzheim, L.; Mattheck, C. SKO (soft kill option): The biological way to find an optimum structure topology. *Int. J. Fatigue* **1992**, *14*. [\[CrossRef\]](#)
- Tovar, A. Bone Remodeling as a Hybrid Cellular Automaton Process. Ph.D. Thesis, University of Notre Dame, South Bend, IN, USA, 2004.
- Svanberg, K. The method of moving asymptotes—A new method for structural optimization. *Int. J. Numer. Methods Eng.* **1987**, *24*, 359–373. [\[CrossRef\]](#)
- Ananthasuresh, G.; Kota, S.; Gianchandani, Y. A methodical approach to the design of compliant micromechanisms. *Solid-State Sens. Actuator* **1994**, 189–192. [\[CrossRef\]](#)
- Sigmund, O. On the design of compliant mechanisms using topology optimization. *Mech. Struct. Mach.* **1997**, *25*, 493–524. [\[CrossRef\]](#)
- Zhu, B.; Zhang, X.; Zhang, H.; Liang, J.; Zang, H.; Li, H.; Wang, R. Design of compliant mechanisms using continuum topology optimization: A review. *Mech. Mach. Theory* **2020**. [\[CrossRef\]](#)
- Pedersen, C.B.W.; Buhl, T.; Sigmund, O. Topology synthesis of large-displacement compliant mechanisms. *Int. J. Numer. Methods Eng.* **2001**, 2683–2705. [\[CrossRef\]](#)
- Wehrle, E.J.; Han, Y.H.; Duddeck, F. Topology optimization of transient nonlinear structures—A comparative assessment of methods. In Proceedings of the 10th European LS-DYNA Conference, Würzburg, Germany, 15–17 June 2015.
- Park, G.J. Technical overview of the equivalent static loads method for non-linear static response structural optimization. *Struct. Multidiscip. Optim.* **2011**, *43*, 319–337. [\[CrossRef\]](#)
- Volz, K.H. Physikalisch begründete Ersatzmodelle für die Crashtoptimierung von Karosseriestrukturen in frühen Projektphasen. Ph.D. Thesis, Technische Universität München, Fachgebiet Computational Mechanics, Munich, Germany, 2011.
- Duddeck, F.; Volz, K. A new topology optimization approach for crashworthiness of passenger vehicles based on physically defined equivalent static loads. In Proceedings of the International Crashworthiness Conference, Milan, Italy, 18–20 July 2012.
- Duddeck, F.; Hunkeler, S.; Lozano, P.; Wehrle, E.; Zeng, D. Topology optimization for crashworthiness of thin-walled structures under axial impact using hybrid cellular automata. *Struct. Multidiscip. Optim.* **2016**, *54*, 415–428. [\[CrossRef\]](#)
- Dirksen, F.; Berg, T.; Lammering, R.; Zohdi, T.I. Topology synthesis of large-displacement compliant mechanisms with specific output motion paths. *Proc. Appl. Math. Mech.* **2012**, 801–804. [\[CrossRef\]](#)
- Chen, Q.; Zhang, X.; Zhu, B. A 213-line topology optimization code for geometrically nonlinear. *Struct. Multidiscip. Optim.* **2019**, *59*, 1863–1879. [\[CrossRef\]](#)
- Stainko, R. An adaptive multilevel approach to the minimal compliance problem. *Commun. Numer. Methods Eng.* **2005**, *22*, 109–118. [\[CrossRef\]](#)
- de Sturler, E.; Paulino, G.; Wang, S. Topology Optimization with Adaptive Mesh Refinement. In Proceedings of the 6th International Conference on Computation of Shell and Spatial Structures, Ithaca, NY, USA, 28–31 May 2008;
- Borrvall, T.; Petersson, J. Large-scale topology optimization in 3D using parallel computing. *Comput. Methods Appl. Mech. Eng.* **2001**, *190*, 6201–6229. [\[CrossRef\]](#)
- Nguyen, T.H.; Paulino, G.H.; Song, J.; Le, C.H. A computational paradigm for multiresolution topology optimization (MTOP). *Struct. Multidiscip. Optim.* **2010**, *41*, 525–539. [\[CrossRef\]](#)
- Nguyen, T.H.; Paulino, G.; Song, J.; Le, C.H. Improving multiresolution topology optimization via multiple discretizations. *Int. J. Numer. Methods Eng.* **2012**, *92*, 507–530. [\[CrossRef\]](#)
- Duysinx, P.; Sigmund, O. New developments in handling stress constraints in optimal material distributions. In Proceedings of the 7th AIAA/USAF/NASA/ISSMO Symposium on Multidisciplinary Design Optimization, Saint Louis, MO, USA, 2–4 September 1998.
- De Leon, D.M.; Alexandersen, J.; Fonseca, J.S.O.; Sigmund, O. Stress-constrained topology optimization for compliant mechanism design. *Struct. Multidiscip. Optim.* **2015**, *52*, 929–943. [\[CrossRef\]](#)

29. Conlan-Smith, C.; James, K.A. A stress-based topology optimization method for heterogeneous. *Struct. Multidiscip. Optim.* **2019**, *60*, 167–183. [[CrossRef](#)]
30. De Leon, D.M.; Gonçalves, J.F.; de Souza, C.E. A Study on the Design of Large Displacement Compliant Mechanisms with a Strength Criteria Using Topology Optimization. In *Advances in Structural and Multidisciplinary Optimization*; Schumacher, A., Viator, T., Fiebig, S., Bletzinger, K.U., Maute, K., Eds.; Springer International Publishing: Cham, Switzerland, 2018; pp. 952–966.
31. Kreisselmeier, G.; Steinhauser, R. Systematic control design by optimizing a vector performance vector. In Proceedings of the International Federation of Active Controls Symposium on Computer-Aided Design of Control Systems, Zürich, Switzerland, 29–31 August 1979.
32. Yang, R.J.; Chen, C.J. Stress-based topology optimization. *Struct. Optim.* **1996**, *12*, 98–105. [[CrossRef](#)]
33. Martins, J.R.R.A.; Poon, N.M.K. On structural optimization using constraint aggregation. In Proceedings of the 6th World Congress on Structural and Multidisciplinary Optimization, Rio de Janeiro, Brazil, 30 May–3 June 2005.
34. Le, C.; Norato, J.; Bruns, T.; Ha, C.; Tortorelli, D. Stress-based topology optimization for continua. *Struct. Multidiscip. Optim.* **2010**, *41*, 605–620. [[CrossRef](#)]
35. Verbart, A.; Langelaar, M.; Keulen, F.V. A unified aggregation and relaxation approach for stress-constrained topology optimization. *Struct. Multidiscip. Optim.* **2017**, *55*, 663–679. [[CrossRef](#)]
36. Crisfield, M. *Non-Linear Finite Element Analysis of Solids and Structures*, 1st ed.; Essentials; Wiley: Hoboken, NJ, USA, 1996; Volume 1.
37. Kim, N.H. *Introduction to Nonlinear Finite Element Analysis*; Springer: Berlin/Heidelberg, Germany, 2015.
38. Reinisch, J. Topologieoptimierung von Compliant Mechanisms mit Nichtlinearer FEM und Spannungsrestriktionen. Semester Thesis, Lehrstuhl für Leichtbau, Technische Universität München, Munich, Germany, 2017.
39. Reinisch, J. Synthesis of Compliant Mechanisms for Morphing Wings with Nonlinear Topology Optimization. Master's Thesis, Lehrstuhl für Luftfahrtsysteme, Technische Universität München, Munich, Germany, 2019.
40. Grosse, N. Nonlinear Topology Optimization with Compressible Hyperelastic Material Models. Master's Thesis, Lehrstuhl für Luftfahrtsysteme, Technische Universität München, Munich, Germany, 2019.
41. Sigmund, O. Morphology-based black and white filters for topology optimization. *Struct. Multidiscip. Optim.* **2007**, *33*, 401–424. [[CrossRef](#)]
42. Bruns, T.E.; Tortorelli, D.A. Topology optimization of non-linear elastic structures and compliant mechanisms. *Comput. Methods Appl. Mech. Eng.* **2001**, *190*, 3443–3459. [[CrossRef](#)]
43. Guest, J.K.; Prevost, J.H.; Belytschko, T. Achieving minimum length scale in topology optimization using nodal design variables and projection functions. *Int. J. Numer. Methods Eng.* **2004**, *61*, 238–254. [[CrossRef](#)]
44. Bruns, T.E.; Tortorelli, D.A. An element removal and reintroduction strategy for the topology optimization of structures and compliant mechanisms. *Int. J. Numer. Methods Eng.* **2003**, *57*, 1413–1430. [[CrossRef](#)]
45. Yoon, G.H.; Kim, Y.Y. Element connectivity parameterization for topology optimization of geometrically nonlinear structures. *Int. J. Solids Struct.* **2005**, *42*, 1983–2009. [[CrossRef](#)]
46. Wang, F.; Lazarov, B.; Sigmund, O. On projection methods, convergence and robust formulations in topology optimization. *Struct. Multidiscip. Optim.* **2011**, *43*, 767–784. [[CrossRef](#)]
47. Wang, F.; Lazarov, B.S.; Sigmund, O.; Jensen, J.S. Interpolation scheme for fictitious domain techniques and topology optimization of finite strain elastic problems. *Comput. Methods Appl. Mech. Eng.* **2014**, *276*, 453–472. [[CrossRef](#)]
48. Martins, J.R.R.A.; Hwang, J.T. Review and unification of methods for computing derivatives of multidisciplinary computational models. *AIAA J.* **2013**, *51*, 2582–2599. [[CrossRef](#)]
49. Bliss, G.A. *Mathematics for Exterior Ballistics*; Wiley: Hoboken, NJ, USA, 1944.
50. Goodman, T.R.; Lance, G.N. The numerical integration of two-point boundary value problems. *Math. Tables Other Aids Comput.* **1956**, *10*, 82–86. [[CrossRef](#)]
51. Kelley, H.J. Method of gradients. In *Optimization Techniques—With Applications to Aerospace Systems*; Academic Press: Cambridge, MA, USA, 1962; pp. 205–254.
52. Michaleris, P.; Tortorelli, D.A.; Vidal, C.A. Tangent operators and design sensitivity formulations for transient non-linear coupled problems with applications to elastoplasticity. *Int. J. Numer. Methods Eng.* **1994**, *37*, 2471–2499. [[CrossRef](#)]
53. Tortorelli, D.A.; Michaleris, P. Design sensitivity analysis: Overview and review. *Inverse Probl. Eng.* **1994**, *1*, 71–105. [[CrossRef](#)]
54. Achleitner, J.; Rohde-Brandenburger, K.; Hornung, M. Airfoil optimization with CST parameterization for (un-) conventional demands. In Proceedings of the XXXIV Congress of the International Scientific and Technical Organisation for Gliding, Hosín, Czech Republic, 28 July–2 August 2018; pp. 117–120.
55. Achleitner, J.; Rohde-Brandenburger, K.; Rogalla von Bieberstein, P.; Sturm, F.; Hornung, M. Aerodynamic design of a morphing wing sailplane. In Proceedings of the AIAA Aviation 2019 Forum, Dallas, TX, USA, 14 June 2019; doi:10.2514/6.2019-2816. [[CrossRef](#)]
56. Sturm, F.; Achleitner, J.; Jocham, K.; Hornung, M. Studies of anisotropic wing shell concepts for a sailplane with a morphing forward wing section. In Proceedings of the AIAA Aviation 2019 Forum, Dallas, TX, USA, 14 June 2019; doi:10.2514/6.2019-2817. [[CrossRef](#)]
57. Bluhm, G.; Sigmund, O.; Poulis, K. Internal Contact Modeling for Finite Strain Topology Optimization. *Comput. Mech.* **2021**, *74*. [[CrossRef](#)]